Bulletin of the Seismological Society of America, Vol. 108, No. 4, pp. 2046–2053, August 2018, doi: 10.1785/0120170315

Array-Based Earthquake Location for Regional Earthquake Early Warning: Case Studies from the Dead Sea Transform

by Andreas S. Eisermann, Alon Ziv, and Hillel G. Wust-Bloch

Abstract Constraining earthquake locations with as few stations as possible is crucial for earthquake early warning. In this study, a new real-time array-based location algorithm is introduced that consists of two modules. The first is a single standalone array module that monitors waveform slowness and back azimuth in a continuous manner and identifies *P*- and *S*-phase arrivals. The second is a multiarray module that intersects multiple back-azimuth estimates and surfaces of equal differential arrivals of the *P* phase. Initial location estimates are issued either by the standalone module, after the *S*-phase arrival to the first array, or by the multiple arrays module after the *P* phase arrives to a second array. Location estimates are subsequently updated with data made available by additional arrays. This approach is validated with 10 earthquakes recorded by small-aperture arrays deployed along the Dead Sea Transform. Use of real-time array methodology is particularly suited to environments with sparse network and/or unfavorable source–station configurations.

Introduction

Earthquake early warning systems (EEWS) are real-time procedures that assess the potential intensity of ground shaking and disseminate alerts (Allen *et al.*, 2009; Bose *et al.*, 2012). Two main types of EEWS are available: regional and onsite. Typically, the former approach is based on *P*-phase attributes at four or more network stations (Satriano *et al.*, 2011; Kuyuk and Allen, 2014), whereas the latter uses a smaller number of stations deployed at the target site. Unlike onsite systems, the ground-motion assessment by regional systems requires hypocenter location, and severe hypocenter mislocation would result in erroneous ground-motion prediction. Thus, a keystone of an effective regional EEWS is a fast and robust hypocenter location. When the network is sparse or, as is often the case, off the source region, hypocenter location may be slow, inaccurate, and ambiguous. Thus, seeking ways to locate off-network earthquakes, resolve ambiguities (Eisermann *et al.*, 2015), and more accurately constrain earthquake locations with less than four network stations is of great interest. Within that context, the potential of array methodologies for EEWS applications stems from their ability to constrain the time evolution of the back azimuth and slowness (Meng *et al.*, 2014). Changes in slowness, together with back azimuth, may then be used to identify phase arrivals, constrain the *S*–*P* interval, and subsequently the epicenter.

In this study, we describe a real-time array-based location algorithm that provides initial location estimate after the *S*-phase arrival to the first array, or after the *P*-phase arrival to a second array. We validate the new approach with 10 earthquakes recorded by small-aperture arrays deployed in the Dead Sea Valley along the Dead Sea Transform (DST), halfway between Amman and Jerusalem (Fig. 1a).

Real-Time Array-Based Location Algorithm

The real-time location algorithm implements principles of array seismology. It consists of two main modules; one for a single standalone array (Fig. 2) and another that integrates information arriving from multiple arrays (Fig. 3). The former monitors waveform slowness and back azimuth in a continuous manner, identifies *P*- and *S*-phase arrivals and outputs back azimuth, epicentral distance, and location estimates. The latter integrates data from multiple standalone modules and intersects multiple back-azimuth estimates with surfaces of equal differential time (EDT) for *P*-phase arrivals.

Single Standalone Array Module

The single standalone array module monitors the back azimuth and slowness of coherent phases. Changes in those parameters are used to identify the *P*- and *S*-phase arrivals, and subsequently the hypocentral distance. The latter, together with the back azimuth and an empirical relation between *S*–*P* and epicentral distance, yields an epicentral location. The module consists of three sets of submodules: the first set (A1–A4) scans continuously on the data, outputs timelines of slowness and back azimuth, and picks the first *P*-phase arrival; the second set (B1 and B2) uses outputs of the first set of submodules to estimate event back azimuth,

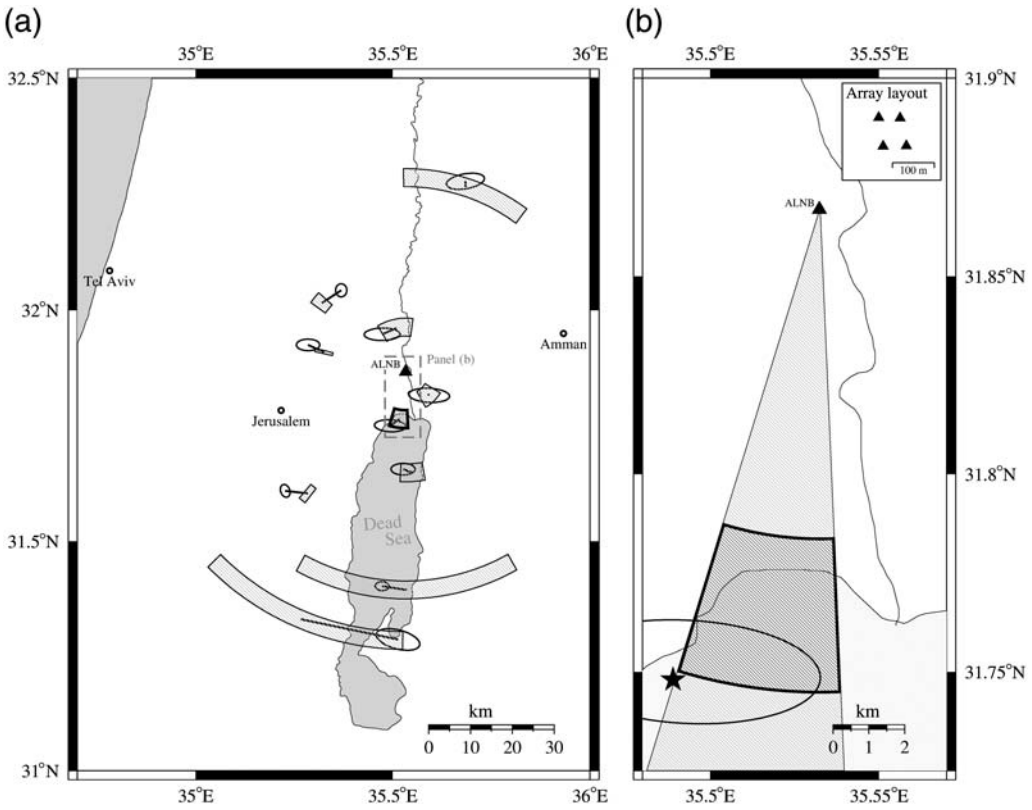

Figure 1. Location maps showing the study area, the array (solid triangles), and the 10 earthquakes analyzed in this study. (a) Comparison between catalog and array-based epicenters, with ellipses and arc sections indicate catalog and array-based location uncertainties, respectively. Dashed rectangle shows the location of (b). (b) The 9 June 2015 M_D2 Kalia earthquake. Star and gray cone indicate the Israel Seismic Network (ISN) catalog location and the back azimuth (BAZ) beam, respectively. The triangle indicates the location of ALNB array, for which the layout is shown in the inset.

initial slowness, and to pick the *S* phase; and the third set (C1 and C2) integrates the available data to constrain hypocentral locations.

Submodule A. Waveform Scanner and P-Phase Picker. This module operates continuously on the data.

A1. Long-time average (LTA) monitor. For each component, it continuously computes the ground-motion root mean square (rms) of the last 5 s of data.

A2. Intersensor time offsets. It computes an intersensor cross-correlation matrix for each component, using a 0.5-s-long moving data window. To resolve the short-time offsets resulting from the very small intersensor aperture (100–300 m), high-sampling rate (500 Hz) and subsample cross-correlation methods are implemented. The submodule outputs the intersensor coherency parameters and time offsets for each component.

A3. Back azimuth and slowness timelines. For each component, it partitions the *N*-sensor array into a set of $N!/[3!(N-3)!]$ three-sensor combinations (Joswig, 2008). For each such combination, it computes the apparent slowness vector via least-squares solution of the following system:

$$\begin{pmatrix} x_{12}^n & x_{12}^e \\ x_{23}^n & x_{23}^e \\ x_{13}^n & x_{13}^e \end{pmatrix} \begin{pmatrix} S_e \\ S_n \end{pmatrix} = \begin{pmatrix} \Delta t_{12} \\ \Delta t_{23} \\ \Delta t_{13} \end{pmatrix}, \tag{1}$$

in which x are the intersensor distances, with subscripts indicating the sensor indexes, S_e and S_n are the east and north components of the slowness, respectively, and Δt are the intersensor time offsets. Next, it computes the scalar slowness (SLO) and the back azimuth (BAZ) according to

$$\mathrm{SLO} = (S_e^2 + S_n^2)^{1/2} \tag{2a}$$

$$\mathrm{BAZ} = \mathrm{atan2}(S_e, S_n). \tag{2b}$$

SLO and BAZ estimates are trustable if the traces are coherent and the set of intersensor time offsets is self-consistent, that is, it satisfies $\Delta t_{12} + \Delta t_{23} = \Delta t_{13}$ (Cansi *et al.*, 1993). Thus, the SLO and BAZ estimates are weight averaged proportionally to

$$W = \begin{cases} \mathrm{CC} \times \mathrm{SC}, & \mathrm{SC} \geq 0.8 \\ 0, & \mathrm{SC} < 0.8 \end{cases}, \tag{3a}$$

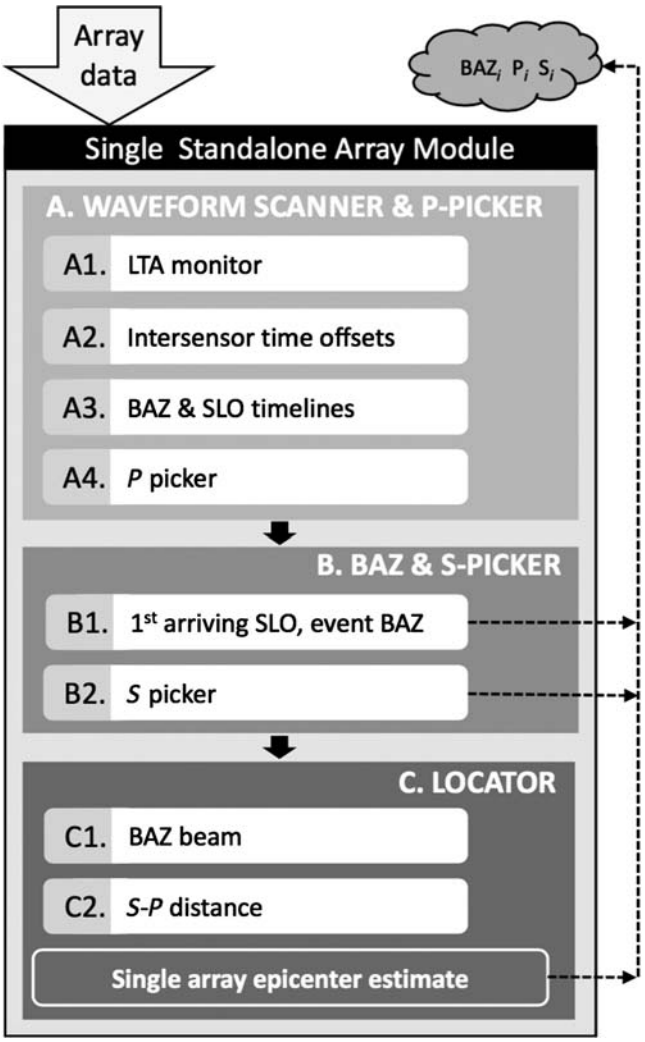

Figure 2. Flowchart for the single standalone array module. LTA, long-time average; SLO, slowness.

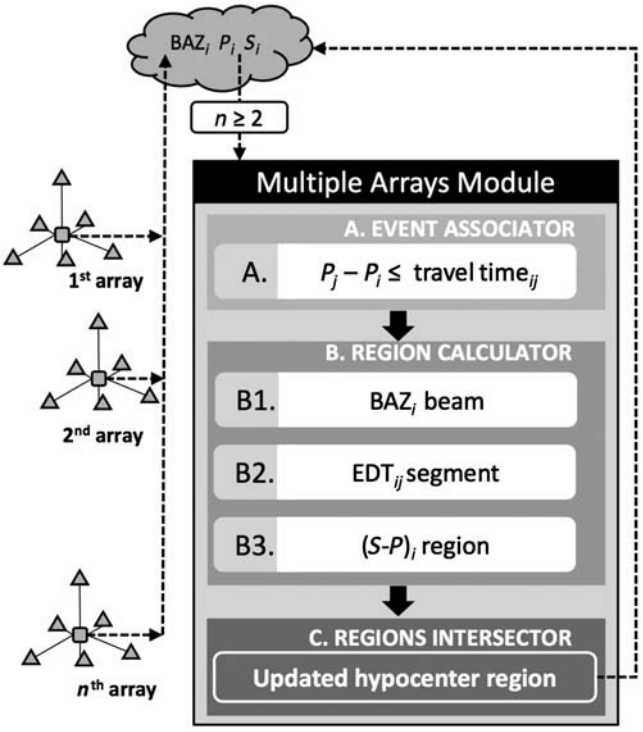

Figure 3. Flowchart for the multiple arrays module.

in which CC is a parameter between 0 and 1 that quantifies the waveforms coherency as

$$\mathrm{CC} = \mathrm{CC}_{12} \times \mathrm{CC}_{23} \times \mathrm{CC}_{13}, \tag{3b}$$

and the SC is a parameter between 0 and 1 that quantifies the self-consistency of the three intersensor time offsets according to

$$\mathrm{SC} = 1 - \frac{\Delta t_{12} + \Delta t_{23} - \Delta t_{13}}{|\Delta t_{12}| + |\Delta t_{23}| + |\Delta t_{13}|}. \tag{3c}$$

In equation (3a), combinations for which SC is less than 0.8 are disregarded. The submodule outputs the weighted-average slowness and back-azimuth estimates corresponding to the component for which the mean W is the highest.

A4. P-phase picker. It picks the *P*-phase arrival once the following four criteria are satisfied: (a) $W \geq 0.5$, (b) the SLO ≤ 0.5 for more than half of the subarray combinations, (c) the current ground motion over the array is at least five times larger than the preceding LTA value, and (d) the vertical rms is larger than the horizontals.

Submodule B. Back Azimuth and S-Phase Picker. The second set of submodules starts once a *P*-phase arrival is declared. It runs the following submodules.

B1. First-arriving slowness and event back azimuth. It time averages the median SLO and BAZ estimates weighted by their W. The averaging interval ends once the BAZ stabilizes (typically less than 0.2 s). It outputs the first-arriving SLO and event BAZ, as well as their observed ranges.

Under poor SNR conditions, the drop to seismic slowness may only occur well after the *P*-phase arrival, during the passage of the *S* waves. In such cases, the submodule only reports an event BAZ and exits.

B2. S-phase picker. It uses the horizontal estimates of A3 and declares *S*-phase arrival if the following two criteria are satisfied: (1) when slowness rises more than 1.5 times the SLO value and (2) when the back azimuth is within ±30° of the observed BAZ.

Submodule C. Locator. The epicentral location is progressively constrained with back azimuth, *S*–*P* interval, and an array-specific empirical relation between the latter and the epicentral distance R (Fig. 4):

$$T_S - T_P = a + bR, \tag{4}$$

in which T_S and T_P are the times of the *S*- and *P*-phase picks, and a and b are station-specific empirical coefficients that are equal to 2 and 0.11, respectively.

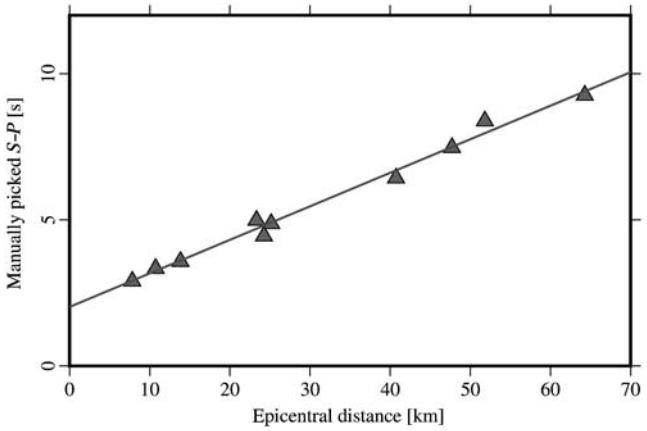

Figure 4. Manually picked *S–P* as a function of epicentral distance, and a least-squares fit to equation (4) with $a = 2$ and $b = 0.11$.

C1. Back-azimuth beam. A back-azimuth beam is formed with the BAZ estimate and an uncertainty corresponding to the observed range.

C2. S–P distance. Once an *S* phase is picked, the hypocenter region is constrained by the width of the BAZ beam at the distance given by the *S–P* arrival-time difference.

For $3 \le N \le 6$, the computation time is negligible and the algorithm is well suited for real-time applications. When the hypocenter is located beneath the array or the event is teleseismic, the wavefront approaches the array subvertically. In such cases, the intersensor delays may be more difficult to resolve. Nevertheless, the SC parameter (equation 3c), which checks for the consistency of the intersensor delays, will indicate whether the result is trustable. If it is not, BAZ and SLO cannot be estimated, and the array functions as a single standard station.

Multiple Arrays Module

When two or more standalone arrays are available, unambiguous epicenter locations may be obtained by intersecting multiple back-azimuth beams with additional available location constraints. Each standalone module runs on a local central processing unit (CPU) at the array site and streams its output to a central server, in which the multiple arrays module integrates the incoming outputs. The multiple arrays module starts once two or more *P*-phase picks become available. It consists of the following submodules.

Submodule A. Event Associator. It associates two *P*-phase picks if the following time–space condition is met:

$$|T_{P_i} - T_{P_j}| \le \frac{R_{ij}}{V_P}, \tag{5}$$

in which the subscripts i and j are the array indexes and R_{ij} is the interarray distance.

Submodule B. Region Calculator. The module starts once the condition in equation (5) is met.

B1. Back-azimuth beam. It calculates a back-azimuth beam as in subroutine C1 of the standalone module.

B2. EDT segment. It computes an EDT region by identifying the set of spatial coordinates η and ξ that satisfies the equality between observed and calculated arrival-time differences:

$$T_{P_i} - T_{P_j} = T_{P_i}^{\mathrm{calc}}(\eta, \xi) - T_{P_j}^{\mathrm{calc}}(\eta, \xi) | i \ne j. \tag{6}$$

Uncertainties in the *P*-phase picking and the velocity model are accounted for as follows: the maximum phase picking uncertainty is set to 20% of the moving data interval (0.1 s), and the maximum velocity model variation is set to ±5% of the 1D 4-layer Israel Seismic Network (ISN) *P*-velocity model (Alderson *et al.*, 2003). Using a standard Monte Carlo approach, these uncertainties are translated into travel-time uncertainties and are mapped onto the EDT surfaces (Eisermann, 2018).

B3. S–P region. Once an *S*-phase pick becomes available, it calculates a spherical region around the array that registered the *S*-phase arrival according to equation (4), for which the thickness accounts for uncertainties in the phase picking and the empirical parameters.

Submodule C. Regions Intersector. According to their order of arrival, BAZ, EDT, and *S–P* constraints are aggregated and intersected to obtain a shrinking hypocenter location with time (Eisermann *et al.*, 2015).

Case Studies from the Dead Sea Transform

The algorithm was tested using data recorded by two standalone small-aperture arrays deployed along the DST, within a sedimentary basin that is 15 km deep and 20 km wide (Garfunkel and Ben-Avraham, 1996). Their location was chosen for their proximity to the epicenter of the 11 July 1927 M_L 6.25 Jericho earthquake, the most recent destructive earthquake along the DST. Presently, the DST is locked down to 15 km and slips 5 mm/yr at greater depth (Sadeh *et al.*, 2012). Several factors impede hypocentral depth determination: the lack of a 3D velocity model, the network sparseness, and the asymmetric network layout with respect to the DST. Nevertheless, based on the intercept of the *S*-minus-*P* as a function of epicentral distance curve (Fig. 4), the possibility of hypocenters deeper than 12 km can be ruled out.

The northern ALNB array consists of three 3D short-period (SP) and one 1D SP sensors, deployed in a square-shape geometry (inset of Fig. 1b) with a maximum aperture of 100 m. The OVNT array, with an aperture of 210 m, is located 23 km to the south of ALNB. It has one 3D SP and five 1D SP sensors. Future use of these arrays for EEWS applications will require fitting them with 3D strong-motion sensors. Data recorded by these arrays are acquired in continuous mode at 500 Hz. While ALNB operated almost

uninterruptedly since 2015, OVNT was deployed later, in fall 2016, and has a smaller incomplete database of local earthquakes. Additionally, because OVNT has only one 3D sensor, it cannot pick the *S*-phase arrival and therefore cannot provide a single-station hypocentral region. First, ALNB data are used to test the single array module, then ALNB and OVNT data are integrated to validate the multiarray module.

Single Array Locations

The single standalone array module was tested in offline mode with 25 months of data recorded by ALNB. The algorithm detected then computed BAZ and *S–P* estimates for 10 local earthquakes ($1.7 \leq \mathbf{M} \leq 4.4$) that are reported by the ISN catalog (see Table 1). These earthquakes provide a complete azimuthal coverage around ALNB. A plot of BAZ discrepancies as a function of catalog BAZ (dark-gray triangles in Fig. 5a) reveals an average absolute discrepancy of less than 10° between array-based and catalog BAZ, with an average uncertainty (indicated by black vertical lines) of about 13°. It is emphasized that the discrepancies reported on this diagram are not only due to the limitations of the real-time algorithm and of the array aperture, but also due to the large ISN location uncertainties resulting from poorly resolved velocity model for the Dead Sea basin and its complex subsurface. The lack of trend in Figure 5a confirms that azimuthal bias due to local subsurface structure (Meng *et al.*, 2014) or array configuration may be ruled out. A comparison between BAZ estimates obtained with the real-time algorithm (dark-gray triangles in Fig. 5a) and with a standard $f-k$ analysis in 1–10 Hz frequency range (light-gray triangles in Fig. 5a) indicates a better performance of the former. Indeed, partitioning the array into three-sensor combinations allows identifying and discarding inconsistent and poor quality estimates, thus enhancing the robustness of the real-time algorithm. A plot of the *S–P* discrepancies as a function of the manually picked *S–P* intervals (Fig. 5b) indicates an average discrepancy of approximately 0.2 s between array-based and manually picked *S–P* values, with a maximum discrepancy of 0.5 s.

Table 1
List of Earthquakes

Date (yyyy/mm/dd)	Time (hh:mm:ss.ss)	Latitude (°)	Longitude (°)	M_D
2015/05/20	03:26:50.97	32.044	35.366	1.7
2015/05/21	01:23:23.42	31.814	35.587	2.1
2015/06/09	20:59:21.92	31.748	35.489	2.0
2015/07/29	22:25:42.94	31.949	35.472	2.0
2015/07/30	02:39:05.83	31.403	35.471	4.4
2015/08/15	07:39:48.57	31.288	35.506	3.1
2016/03/06	22:55:03.87	31.927	35.286	2.0
2017/01/06	05:15:47.22	32.278	35.682	3.2
2017/05/23	22:58:49.37	31.609	35.227	2.0
2017/06/02	12:19:48.72	31.657	35.526	2.1

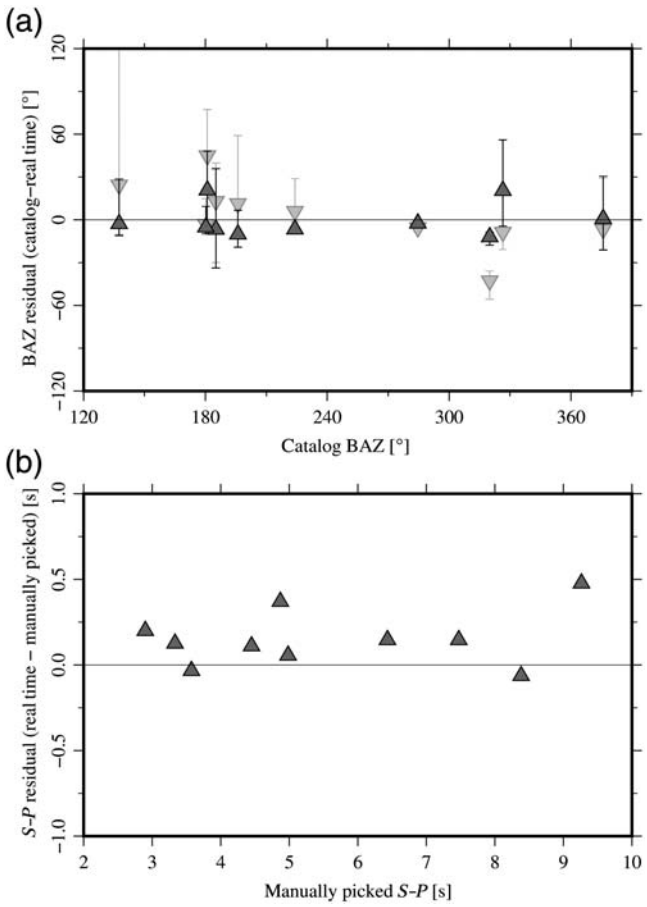

Figure 5. Algorithm validation with 10 earthquakes. (a) BAZ residuals (catalog minus array based) as a function of catalog BAZ, with vertical lines indicating range of BAZ estimates obtained in step B1 of the algorithm. Real-time and standard $f-k$ estimates are indicated by dark-gray and light-gray triangles, respectively. (b) *S–P* residuals (real time minus manually picked) as a function of manually picked *S–P*, with uncertainty range of 0.5 s resulting from the width of the moving window.

Manually picked *S–P* intervals as a function of the ISN epicentral distances are shown in Figure 4, along with a linear best-fitting curve (epicentral rather than hypocentral distances are used, because the catalog depth uncertainties are large with respect to the epicentral distances considered here). Uncertainties in the *S–P* intervals, empirical *S–P* versus distance relation and BAZ estimates are mapped into location uncertainties (Fig. 1a). Out of the 10 single array-based locations, 7 results lie well within the uncertainty limits of ISN locations (black ellipses), and the remaining 3, with array-source distances exceeding 50 km, are located within less than 5 km from the ISN locations. It is thus concluded that the algorithm introduced in this study provides reliable real-time location estimates, using exclusively data from a single standalone array. As it is for standard regional EEWS, the effectiveness of the real-time array-based location depends on the epicenter-array-target configuration. A necessary condition for timely warnings is that the array-

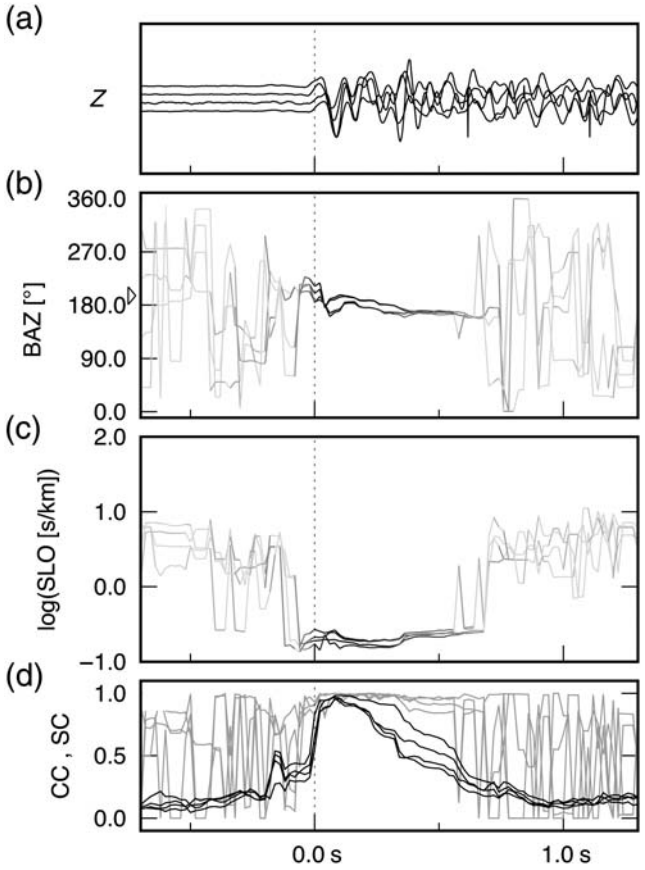

Figure 6. Seismograms and module A3 outputs of the 9 June 2015 M_D 2 earthquake. (a) Two seconds of *P*-wave vertical-component waveforms. Timelines of (b) BAZ, (c) SLO, and (d) CC (black) and SC (gray) estimates for each of the three-sensor combinations. The vertical dashed line indicates the *P*-phase picking. The gray scale of the BAZ and SLO curves is proportional to *W*. With the arrival of the signal, the spread of the four BAZ and SLO estimates diminishes, and SC and CC approach unity.

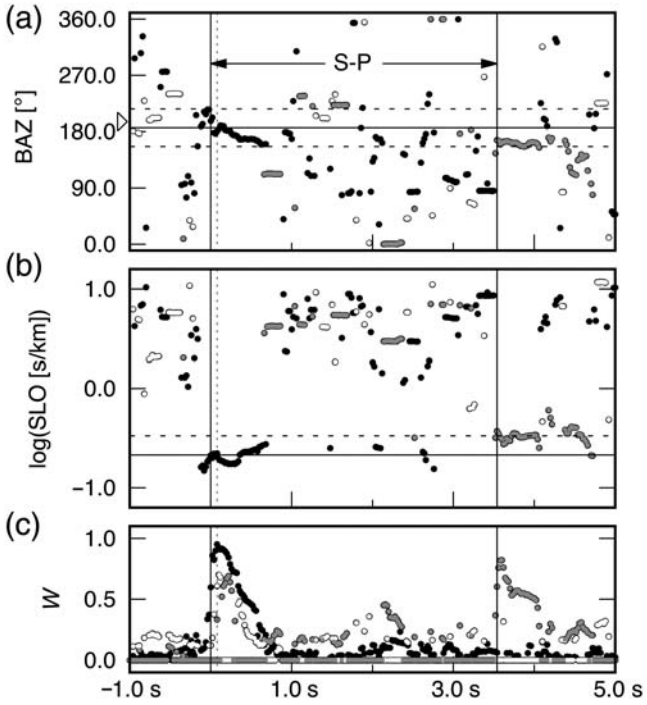

Figure 7. Timelines of weighted average BAZ, SLO, and *W* of the 9 June 2015 M_D 2 earthquake. (a) BAZ estimates, with a vertical dashed line indicating the end of the 0.1 s interval used to obtain a stable BAZ estimate. The triangle adjacent to the ordinate indicates the catalog BAZ and the horizontal solid line indicates array-based BAZ. The two horizontal dashed lines outline the BAZ criterion for *S*-phase picking (see module B2). (b) SLO estimates. Horizontal solid and dashed lines indicate *P*-phase SLO and the SLO-criterion for *S*-phase picking, respectively. (c) Mean *W*, with black, white, and gray symbols corresponding to vertical, east, and north components, respectively. The two vertical solid lines indicate the *P*- and *S*-phase picks.

to-epicenter distances should be shorter than those of the epicenter-to-target. With respect to Amman, this warning condition is satisfied for 9 out of the 10 earthquakes, and for Jerusalem 6 times (Fig. 1a).

Example timelines of BAZ, SLO, and *W* are now examined for the 9 June 2015 M_D2 earthquake, for which the epicenter is indicated by the black star in Figure 1b. Because the array aperture is small and site effects are uniform, the waveforms exhibit high similarity, and the cross-correlation approach yields robust intersensor time offsets (Fig. 6). Prior to the *P*-phase arrival (vertical dashed line in Fig. 6), the BAZ and SLO estimates obtained for each three-sensor combinations are highly variable and nonstable. Shortly after the *P*-phase pick, these estimates converge into a narrowband (Fig. 6b,c), and the combination-specific CC and SC stabilize initially very close to their maximal value of 1 (Fig. 6d). Recall that combinations with SC less than 0.8 are disregarded (equation 3a). Timelines of mean BAZ, SLO, and *W* are shown in Figure 7 for a 6-s-long interval that includes the *P*- and *S*-phase picks (vertical solid lines). Prior to the *P*-phase pick, the mean *W* is low, and consequently both BAZ and SLO estimates are highly variable. The arrival of the *P*-phase (first vertical line) is accompanied by an abrupt rise in the mean *W*. This increase is apparent in all three components but is stronger (close to 1) in the vertical component (black symbols) than in the horizontal components (white and gray symbols). The mean *W* corresponding to the vertical component remains above the horizontal values for 1 s, during which both BAZ and SLO are highly stable. The array-based BAZ (solid horizontal line in Fig. 7a) is in good agreement with the catalog BAZ (triangle adjacent to the ordinate of Fig. 7a), and the observed SLO (solid horizontal line in Fig. 7b) is consistent with that of steeply approaching *P* waves. This *P*-phase SLO value is multiplied by the V_P/V_S ratio to serve as a baseline (horizontal dashed line in Fig. 7b) for further *S*-phase identification. The mean *W* picks up again after about 3.5 s, BAZ stabilizes back to previous values, and SLO rises gradually above the *P*-phase value (horizontal solid line in Fig. 7b). An *S*-phase arrival is declared once the SLO reaches the expected *S*-phase slowness. About 0.2 s after the *P* phase is picked by the ALNB array, a

BAZ estimate (gray hatched zone) is available that points toward the epicenter (black star) (Fig. 1b). The final uncertainty-based epicentral estimate (black hatched zone), which is declared at the time of the *S*-phase pick (at 3.7 s), overlaps with the catalog location uncertainty ellipse (Fig. 1b).

Multiple Arrays Location

The performance of the multiple array module, which aggregates all available constraints in real time, is now demonstrated for the earthquake examined in the preceding section (Fig. 8). The 9 June 2015 M_D 2 earthquake is initially detected by OVNT and a northeast pointing BAZ is obtained 0.2 s after the *P* phase is picked (Fig. 8a). About 0.7 s later, a *P* phase is picked at ALNB, instantaneously delimiting an EDT zone, for which the thickness accounts for picking, velocity model, and depth uncertainties (Fig. 8b). After another 0.2 s, a second BAZ beam is computed at ALNB that points toward OVNT (Fig. 8c). The intersection of the two BAZ beams with the EDT zone provides an unambiguous epicentral zone that overlaps well with that of the ISN catalog. At that time, 1.1 s after the first detection at OVNT, the *P*-phase front (dashed circle in Fig. 8c) is 2–3 s away from Jerusalem and Amman. The *S*-wave front, which has not yet reached the surface, will take an additional 8 or 11 s before hitting Jerusalem and Amman, respectively. Interestingly, the dimension of the hypocentral region constrained by these two arrays is equivalent to that of the standalone module using data from ALNB only (Fig. 1a). In this example, however, because the standalone module waits for the *S*-phase arrival, it would take an additional 2.6 s for the standalone module to output a hypocentral zone.

Summary

A new array-based algorithm for real-time epicenter determination is introduced that consists of two modules. The first is a single standalone array module that monitors waveform slowness and back azimuth in a continuous manner and identifies *P*- and *S*-phase arrivals. It runs on a local CPU at the array site and outputs only key location parameters in real time, thus keeping data traffic to a minimum. The second is a multiarray module that intersects multiple back-azimuth estimates and EDT zones. Initial location estimates are issued either by the standalone module, after the *S*-phase arrival to the first array, or by the multiple arrays module after the *P*-phase arrives to a second array—whichever occurs first.

The single standalone array module is validated with 10 earthquakes ($1.7 \leq \mathbf{M} \leq 4.4$) recorded by a small-aperture array deployed along the DST. Epicentral locations based on a single array show good agreement with the ISN catalog location uncertainty ellipses. Using the multiple array module, it is then shown how the aggregation of BAZ, EDT, and *S–P* estimates, successively available from further arrays, yields robust locations. Use of this real-time array methodology is particularly suited to environments with sparse network and/or unfavorable source–station configurations (e.g., at network boundaries).

Although the BAZ determination and acoustic-versus-seismic discrimination are robust, one can imagine scenarios in which the algorithm returns erroneous *S–P* interval. For example, it may skip the *P* phase and be triggered by the *S* phase. Because, however, this situation did not occur even once in a data set of 10 weak earthquakes, the likelihood of triggering by *S* phase for earthquakes that may be of interest for EEW seems rather small. Furthermore, during large

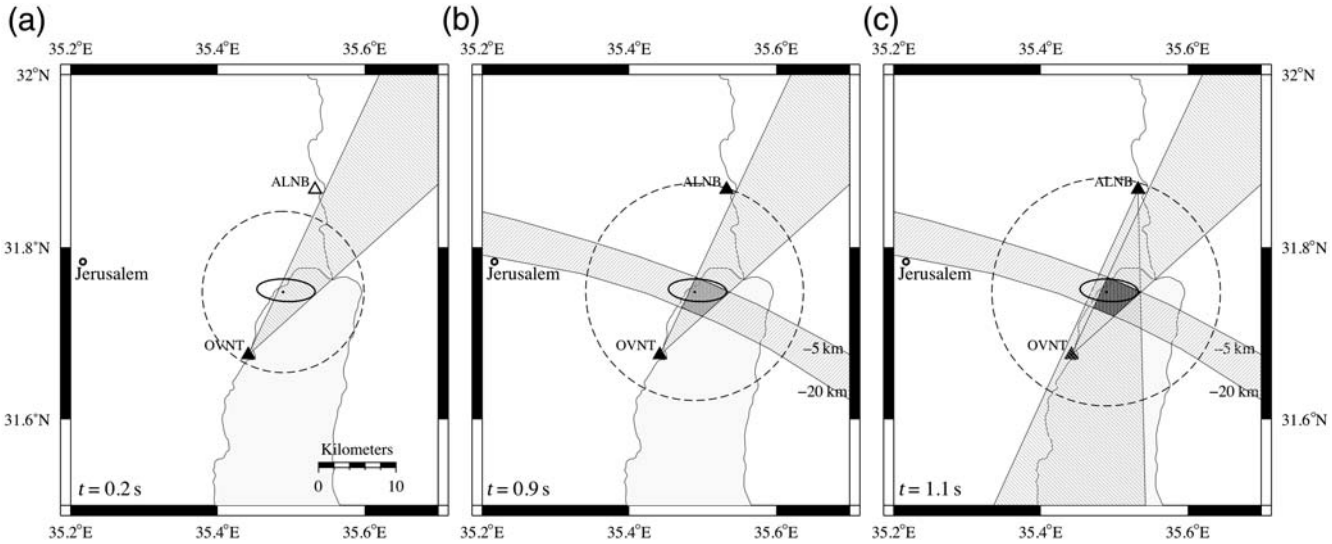

Figure 8. Application of the multiple array module to the 9 June 2015 M_D2 earthquake. (a) The *P* phase is initially detected by OVNT and a BAZ is obtained 0.2 s later. (b) About 0.7 s later, a *P* phase is picked at ALNB, and an EDT zone is immediately available. (c) After another 0.2 s, a second BAZ beam is computed at ALNB that intersects with the first BAZ.

earthquakes, when the rupture duration is larger than the *S–P* interval, the arrival of the earliest *S* phases emitted from the rupture may get contaminated by later *P* phases, thus preventing reliable *S*-phase picking. It is consequently recommended to wait for a second trigger (by an array or a standard station) before issuing alerts. Once a second trigger is available, robust locations may be constrained by intersecting three independent constraints, two BAZ estimates, and one EDT surface.

The array-based location methodology comprises modular algorithms that integrate real-time information arriving from multiple standalone arrays. Epicentral locations are gradually constrained by aggregating parameters (BAZ, EDT, and *S–P*) as they are made available. Once the location is determined, assessing the source magnitude (Lancieri *et al.*, 2011; Sadeh *et al.*, 2014) and predicting the ground-shaking intensity (Lior *et al.*, 2016; Lior and Ziv, 2017) are relatively straightforward. However, practical constraints may hinder the implementation of array-based EEWS, mainly the additional cost incurred by the addition of sensors around standard stations. An elegant solution would consist in deploying a series of low-cost microelectromechanical systems (MEMS) accelerometers around existing seismic stations.

Data and Resources

The DeadSeaNet data (seismograms in miniSEED format and array coordinates) can be downloaded from http://www.deadseanet.org/files/2018_BSSA_ABELFREEW_data.zip (last accessed May 2018).

Acknowledgments

The authors thank Associate Editor Stefano Parolai and two anonymous reviewers for their constructive remarks. This research was supported by Grant Number 2014356 from the United States–Israel Binational Science Foundation (BSF).

References

Alderson, F., Z. Ben-Avraham, A. Hofstetter, E. Kissling, and T. Al-Yazjeen (2003). Lower-crustal strength under the Dead Sea basin from local earthquake data and rheological modeling, *Earth Planet. Sci. Lett.* **214,** 129–142, doi: 10.1016/S0012-821X(03)00381-9.

Allen, R. M., P. Gasparini, O. Kamigaichi, and M. Bose (2009). The status of earthquake early warning around the world: An introductory overview, *Seismol. Res. Lett.* **80,** 682–693.

Bose, M., T. Heaton, and E. Hauksson (2012). Rapid estimation of earthquake source and ground-motion parameters for earthquake early warning using data from a single three-component broadband or strong-motion sensor, *Bull. Seismol. Soc. Am.* **102,** 738–750.

Cansi, Y., J.-L. Plantet, and B. Massinon (1993). Earthquake location applied to a mini-array: k-spectrum versus correlation method, *Geophys. Res. Lett.* **20,** 1819–1822.

Eisermann, A. S. (2018). Earthquake location by distinct constraints for sparse and doubtful data, *Ph.D. Thesis*, Universität Stuttgart.

Eisermann, A. S., A. Ziv, and G. H. Wust-Bloch (2015). Real-time back azimuth for earthquake early warning, *Bull. Seismol. Soc. Am.* **105,** no. 4, doi: 10.1785/0120140298.

Garfunkel, Z., and Z. Ben-Avraham (1996). The structure of the Dead Sea basin, *Tectonophysics* **266,** 155–176.

Joswig, M. (2008). Nanoseismic monitoring fills the gap between microseismic networks and passive seismic, *First Break* **26,** no. 6, 121–128.

Kuyuk, H. S., and R. M. Allen (2014). Designing a network-based earthquake early warning algorithm for California: ElarmS-2, *Bull. Seismol. Soc. Am.* **104,** 162173, doi: 10.1785/0120130146.

Lancieri, M., A. Fuenzalida, S. Ruiz, and R. Madariaga (2011). Magnitude scaling of early-warning parameters for the M_w 7.8 Tocopilla, Chile, earthquake and its aftershocks, *Bull. Seismol. Soc. Am.* **101,** no. 2, 447–463.

Lior, I., and A. Ziv (2017). The relation between ground acceleration and earthquake source parameters: Theory and observations, *Bull. Seismol. Soc. Am.* **107,** no. 2, doi: 10.1785/0120160251.

Lior, I., A. Ziv, and R. Madariaga (2016). *P*-wave attenuation with implications for earthquake early warning, *Bull. Seismol. Soc. Am.* **106,** 13–22, doi: 10.1785/0120150087.

Meng, L., R. M. Allen, and J.-P. Ampuero (2014). Application of seismic array processing to earthquake early warning, *Bull. Seismol. Soc. Am.* **104,** 2553–2561, doi: 10.1785/0120130277.

Sadeh, M., Y. Hamiel, A. Ziv, Y. Bock, P. Fang, and S. Wdowinski (2012). Crustal deformation along the Dead Sea transform and the Carmel fault inferred from 12 years of GPS measurements, *J. Geophys. Res.* **117,** no. B08410, doi: 10.1029/2012JB009241.

Sadeh, M., A. Ziv, and H. Wust-Bloch (2014). Real-time magnitude proxies for earthquake early warning in Israel, *Geophys. J. Int.* **196,** no. 2, 939–950.

Satriano, C., L. Elia, C. Martino, M. Lancieri, A. Zollo, and G. Iannaccone (2011). PRESTo, the earthquake early warning system for Southern Italy: Concepts, capabilities and future perspectives, *Soil Dynam. Earthq. Eng.* **31,** no. 2, doi: 10.1016/j.soildyn.2010.06.008.

Department of Geophysics
Tel-Aviv University
Ramat-Aviv
Tel-Aviv 69978
Israel
eisermann@tau.ac.il

Manuscript received 18 October 2017;
Published Online 15 May 2018